SUPPLEMENTARY MATERIALS AND METHODS

Cell culture

Spirostomum media was made by boiling 1 L of spring water (Carolina Biological Item #132450) with 10 wheat seeds (Carolina Biological Item #132425) and a few leaves of Timothy hay (Carolina Biological Item #132385)[1]. We obtained initial *Spirostomum ambiguum* cultures from Carolina Biological (Item #131590) (confirmed by scientists there to be *Spirostomum ambiguum*). New cultures were made by inoculating media with cells from a mature culture. Mature cultures that had at least two weeks to grow were used for all experiments, since after this time the *Spirostomum* organisms we observed were longer and more consistent in appearance than those of cultures recently inoculated.

Fixation and immunoflorescence microscopy

Cells were fixed with two methods, slow PHEM-formaldehyde and fast EGTA-Methanol fixation.

PHEM-formaldehyde fixation

Cells were transferred from cultures into a 96-well plate and washed with spring water twice. To obtain elongated samples, cells were incubated in 200 µL of 0.5X PHEM buffer (1X PHEM buffer: 60 mM PIPES, 25 mM HEPES, 10 mM EGTA, and 2 mM $MgCl_2$, pH 6.9 [2]) at 4°C for 6 hours, then fixed for 1 hour with 100 µL of 1X PHEM 2% PFA at 4°C. To produce contracted samples, cells were rinsed in 100 µL of 1X PHEM buffer at room temperature (RT) for 15 seconds and fixed with 100 µL of 1X PHEM 2% PFA for 15 minutes. Fixed cells were then treated with 300 µL of 2% PFA 1X PHEM for 60 minutes, and washed three times with 300 µL of permeabilization solution (1X PBS, 3% BSA, and detergent which was either 1% saponin or 0.1% Tween) for 10 minutes each. After fixation, cells were stained for immunofluorescence (see below).

EGTA-Methanol fixation

The second method for fixation was a fast incubation in EGTA in spring water followed by iced methanol fixation. No significant differences were observed between the two sample conditions other than the methanol samples were far more stable to mechanical perturbation, were degraded less by permeabilization, and showed less damage from handling.

Cells were transferred from culture into a 1.5 mL tube and rinsed 3x with spring water. Elongated cells were prepared by exposing the cells to 25 mM EGTA in spring water for about 30 seconds, until the cells no longer contracted in response to mechanical tapping of the tube. Contracted samples skipped this step and went straight to fixation. Cells were then dropped into -80 °C methanol with 2% formaldehyde. Samples were kept at -80 °C for 1 hour, -20 °C for 1 hour, and finally left in 4 °C overnight. Samples were rinsed in 1:1 methanol:PBS, then 3x in PBS. Cells were then transferred to a glass bottom dish (MatTek P35GC-0-14-C) for staining (see below).

Immunofluorescence staining

To visualize cytoskeletal components by immunofluorescence, the following primary antibodies were used: myoneme: 20H5 mouse anti-Centrin (Millipore Sigma, Cat. #04-1624) (previously used to identify centrin in ciliates [3]) or custom Sfi1 antibody (see below); microtubules: TAP952 mouse anti-alpha tubulin (Millipore Sigma, Cat. #MABS277). Cells were incubated in 200 µL primary antibody solution diluted to 10 µL/mL in permeabilization solution, incubated overnight at RT, and washed three times with 300 µL of permeabilization solution for 10 minutes each. Secondary antibodies (ThermoFisher, Cat. #R37115, A11008, and A21244) were diluted 1:1000 in permeabilization solution to make secondary solution. Cells were incubated in 200 µL of secondary solution for three hours at RT, and washed three times with 300 µL of 1X PBS 3% BSA for 10 minutes each before imaging. To stain the cell membrane, cells were incubated in 200 µL 1:1000 CellMask Orange Plasma Membrane Stain (ThermoFisher, Cat #C10045) in PBS for 1 hour and rinsed 3x in PBS before imaging.

For microscopy, stained cells were either transferred onto a glass cover-slip (Neuvitro, Cat. #GG-22-1.5-PLL) with 100 µm spacers (Cospheric, CPMS-0.96 106-125 µm) and a glass slide (VWR, Cat. #16004-430), and sealed with nail polish (Fisher Scientific, Cat. #72180) to prevent evaporation, or samples in a glass bottom dish had a cover-slip placed over the well to prevent evaporation.

Fluorescence imaging

Cells were imaged by immunofluorescence microscopy on the following microscopes:

Elyra:

Base: Zeiss LSM 780
Imaging platform: Elyra PS1 Super-resolution Microscope
Objective: Zeiss Plan-Apochromat 20x/0.8 M27
Modality: Laser Scanning Confocal, Z-stack, Mosaic stitching
Dichroic: MBS 458/514/594
Wavelengths:
Excitation Lasers: 555, 594
Emission Filters: 560-800, 599-734

Dragonfly:

Base: Nikon Ti-E
Imaging platform: Dragonfly Spinning Disk Confocal
Objectives:
- Nikon Plan Fluor 20x/0.75 Mlmm
- Nikon Plan Apo 100x/1.45

Modality: Spinning disk confocal, Z-stack, Mosaic Stitching
Dichroic: Chroma ZT405/488/561/640rpc
Camera: Andor Zyla sCMOS camera
Wavelengths:
Excitation Lasers: 488, 561, 637
Emission Filters: ET525/50m, ET600/50m, ET700/75m

NSPARC:

Base: Nikon Ti2 Eclipse
Imaging platform: AX/AX R NSPARC
Objective: Nikon Plan Apo λD 60x/1.42
Modality: Laser Scanning Confocal (NSPARC), Z-stack, Mosaic Stitching
Dichroic: 405/488/561/640
Wavelengths:
Excitation Lasers: 488, 561, 640
Emission Filters: 502-546nm, 570-616nm, 666-732nm

Sfi1 antibody generation

Custom anti-Sfi1 peptide antibodies (Bethyl Laboratories, Montgomery, TX) were generated for selected peptides identified in *Stentor*. Rabbit preimmune bleeds were first screened to avoid using rabbits that may have been previously exposed to ciliated parasites and already produce antibodies that react with *Stentor* proteins in immunofluorescence. Sfi1 sequence reads were obtained from *Spirostomum* and aligned against *Stentor* Sfi1 to identify homology. The following *Stentor* Sfi1 peptide sequence was identified as having the highest homology to *Spirostomum ambiguum* Sfi1: RTEKLRNALNRVPR. The antibody raised to this peptide was also identified as having a high affinity for *Spirostomum ambiguum* Sfi1 by colocalization in immunofluorescence with centrin (Fig. S1).

Transmission electron microscopy

TEM methods have been adapted from Dykstra and Reuss "Biological Electron Microscopy: Theory, Techniques, and Troubleshooting" and John Kuo "Electron Microscopy: Methods and Protocols" [4, 5].

Fixation and Embedding

Contracted samples were fixed in a fixation buffer of 2.5% glutaraldehyde (EMS Cat # 16220) and either PBS (ThermoFisher Cat# 70011044) or cacodylate buffer (100 mM, pH 7.4) [4]. Samples were first washed three times in spring water. Elongated cells were prepared by exposing the cells to 25 mM EGTA in spring water for about 30 seconds, until the cells no longer contracted in response to mechanical tapping of the tube. Contracted and elongated cells were then taken in a small droplet and dropped into 2 mL of fixation solution and incubated for 2 hours on ice. After fixation, samples were rinsed in buffer without glutaraldehyde and then an ethanol series (50%, 75%, 90%, 100% dilution by volume of ethanol with buffer for 1 hour each) to slowly dehydrate the samples. Samples were left in 100% ethanol overnight before a final rinse in 100% ethanol and then a resin series, where they were left in 50% LR white (EMS CAT# 14380) overnight, then 1 hour each of 75%, 90% then 100% (resin diluted with ethanol); they were then placed in gelatin capsules (EMS CAT# 70110) and baked at 70°C overnight [4].

Microtomy

The samples were microtomed on the Leica UC7 with a glass or diamond knife to a thickness between 70 and 120 nm. The sections were then placed on uncoated 200 mesh nickel grids (EMS CAT# 200-Ni or H200-Ni). We found that the immunolabeled samples prepared using uncoated grids were more fragile and more likely to form holes under the electron beam (as seen in Fig. 3); however, the labeling was far superior, likely due to the two exposed surfaces of the section during staining [6].

Immunogold labeling

Immunogold labeling was performed to label centrin in samples according to EMS protocols [7]. The incubation solution was prepared with 20 mM PBS (Fisher Scientific #BP399500), 0.1% Aurion BSA-C (SKU: 900.099), and 15 mM NaN_3 (CAS 26628-22-8). Following fixation, embedding, and microtomy as described above, the sectioned samples were first washed with 50 mM Glycine (CAS 56-40-6) in PBS for 15 minutes to inactivate any remaining glutaraldehyde, then incubated in goat blocking solution (Aurion SKU: 905.002) for 15 minutes, then rinsed twice in the incubation solution. The grids were then left in 5µ g / ml 20H5 mouse anticentrin antibody (Millipore Sigma, Cat. #04-1624) or Sfi1 antibody (see above) overnight at 4°C. The next day, sections were rinsed five times in incubation solution and then incubated in 1:100 10 nm gold-conjugated secondary antibodies (abcam cat #: ab39619 or Invertrogen Ref: A31566) in incubation solution for 2 hours. The samples were then rinsed five times in the incubation solution, twice in PBS, then post-fixed in 2.5% glutaraldehyde for 15 minutes before being rinsed three times in distilled water. The samples were then stained with 4% uranyl acetate (CAS 541-09-3) for 15 minutes and rinsed three times in distilled water. The samples were then imaged on the Hitachi HT7800 after drying.

Quantification of light and electron microscopy images

Quantitative analysis was carried out primarily using ImageJ Fiji [8]. The lengths and angles obtained from immunofluorescence and TEM were measured using the measurement tools in ImageJ. TEM quantification was performed on the centrin-labeled samples in ImageJ by measuring the fiber width across multiple images and organisms, with 3 embedding repeats and over 10 labeling repeats. The tag density was measured by manual counting of labels on the myoneme and measuring the area over the myoneme in ImageJ, where each point is an average density over a single image. The plots were created using the Python packages matplotlib and seaborn [9, 10]. For each immunofluorescence quantification, measurements from N individual cells (reported for each measurement) were averaged. These cell averages were then in turn averaged to calculate the reported mean and standard error of the mean (SEM) over N samples reported in the figures and text.

Skeletonization analysis

Skeletonization was carried out on the TEM images by first segmenting the structures using Illastik [11]. The images were first reduced in resolution by 4x in each axis. Segmentation used an AI model to separate myoneme structures from the background by hand training the model and making corrections that were fed back into the model. The segmentations were then skeletonized in ImageJ Fiji [8]. The resulting skeletonized images were then processed in a Jupyter notebook with OpenCV [12, 13]. Skeletonized images were first convolved with the following matrix:

$$\begin{bmatrix} 1 & 1 & 1 \\ 1 & 10 & 1 \\ 1 & 1 & 1 \end{bmatrix}.$$

The resulting image could then be classified by the number of neighbors each pixel had. Pixels were classified by value as follows: 11 for end points, 12 for branches, and 13 to 18 for intersection points. Multiple nearby intersections could then be grouped into a single intersection. To pull out edges, a branch traversal algorithm was used to find branches that connected intersections. From these data, we were able to calculate junction angles by counting out 5 pixels from each intersection along a branch and calculating the angle between all of these points from the intersection. The lengths were also calculated for each branch using the Pythagorean theorem to calculate the end-to-end distance between intersections, as well as the total length of the branch by counting pixels along the branch, adding $\sqrt{2}$ for a diagonal step or 1 for an orthogonal step. The lengths were then scaled by the pixel size in nanometers per pixel.

Following skeletonization, branch lengths were fit to a worm-like-chain model to estimate the persistence length of the branches:

$$< L_{E-E}^2 >= 2P^2(\frac{L_{branch}}{P} + e^{\frac{-L_{branch}}{P}} - 1)$$

where L_{E-E} is the end-to-end distance, L_{branch} is the total length, and P is the persistence length [14]

Coarse-grained mesh model

The mesh model was used to simulate three-dimensional changes in organismal shape in response to contraction. The model comprises N points $\mathbf{p}_i$ and an associated energy function $U(\{\mathbf{p}_i\}_{i=1}^N; \mathcal{K})$, where $\mathcal{K}$ represents a set of parameters. To mimic the contraction of the myoneme, which arises from a calcium wave that causes the centrin-based edges of the myoneme to shorten, we assume that calcium activation causes a change in the parameters $\mathcal{K}^{\text{elongated}} \to \mathcal{K}^{\text{contracted}}$. The dynamic aspects of the contraction used in a simplified continuum were studied in Floyd et al. 15. Here we study equilibrated structures following contraction and assume that for a given $\mathcal{K}$, the energy is minimized with respect to the degrees of freedom $\mathbf{p}_i$.

Points $\{\mathbf{p}_i\}_{i=1}^N$ make up a quadrilateral spring mesh that encloses an elongated, cigar-like shape. The mesh is generated using the Catmull-Clark algorithm to subdivide an initial rectangular prism into an iteratively finer surface [16]. The initial prism consists of $n_L = 14$ unit cubes stacked in the z direction (i.e., along the long axis of the cells) and centered on the origin, and points are then added to create progressively smaller quadrilateral faces. We run this process for three iterations (producing $N = 3,714$ points), and, following this initial mesh generation, we scale each coordinate so that the radius of the cylinder is 50 μm. In addition, the entire structure is given a z-dependent rotation, so that each point is rotated in the xy plane by an angle:

$$\theta(z) = \Delta\theta \frac{z - z_{\min}}{z_{\max} - z_{\min}}$$

$\theta(z)$ linearly increases from 0 to $\Delta\theta$ as z increases from the bottom to the top of the structure. We finally apply compression in the z direction to set the total length of the cylinder and so that the angles of the unit cell in the fishnet mesh agree with the measurements on elongated myoneme. The result of this process is the equatorial mesh (Fig. 1E), in which the edges lie along the equators of the cylinder. To produce the fishnet mesh, we move the equatorial edges so that they connect points between two adjacent layers and are offset by one relative to the original longitudinal edges.

Quadrilateral faces define the edges between the points $\mathbf{p}_i$ that are converted to springs in the energy function. We use a Hookean energy function for the spring $u_{ij} = \frac{k_{ij}}{2}(r_{ij} - l_{ij})^2$, with $r_{ij} = ||\mathbf{p}_i - \mathbf{p}_j||$. Before contraction, the rest lengths l_{ij} are set as the initial distance between $\mathbf{p}_i$ and $\mathbf{p}_j$ in the mesh, so that before contraction the

system is in equilibrium. The new rest lengths are set as a factor γ times the original rest length: $l_{ij} \leftarrow \gamma l_{ij}$. The meshes can be made anisotropic by distinguishing between the two sets of springs (equatorial and longitudinal in the latitudinal mesh, and right-handed and left-handed in the fishnet mesh) and assigning different shrinking factors for each direction. To assign the stiffness k_{ij} of each spring, we use the formula $k = EA/l$ where EA is the product of the Young's modulus of the spring material and the cross-sectional area and l is the length of the spring [17]. We assume a fixed value of EA for all springs of a given type and divide by the spring's elongated rest length to obtain k_{ij}. The total spring energy is

$$U_S = \sum_{ij \in \mathcal{E}} \frac{k_{ij}}{2}(r_{ij} - l_{ij})^2 \tag{1}$$

where $\mathcal{E}$ is the set of edges in the mesh.

Because volume V is likely to be conserved during contraction, we constrain volume in the energy function U. We omit the conservation of the surface area here because the area can become ruffled at finer length scales than we resolve in the model (Fig. 1A, C). To calculate the enclosed volume, we create a surface triangulation $\mathcal{T}$ by dividing each quadrilateral face of the equatorial mesh into two oriented triangles. We can pick any point $\mathbf{o}$ in space (for convenience, we choose the origin) and sum the volumes of the tetrahedra that are defined for each face from the four points $\mathbf{o},\ \mathbf{p}_i,\ \mathbf{p}_j,\ \mathbf{p}_k$ [18]. The volume of the tetrahedron is

$$v(t) = \frac{1}{6}(\mathbf{p}_k - \mathbf{o}) \cdot ((\mathbf{p}_i - \mathbf{o}) \times (\mathbf{p}_j - \mathbf{o}))\,. \tag{2}$$

This will have a sign depending on the ordering of i, j, k, so we ensure that the orientation of each triangle t is the same for all $t \in \mathcal{T}$. With this, the total volume is

$$V(\{\mathbf{p}_i\}_{i=1}^N) = \sum_{t \in \mathcal{L}} v(t). \tag{3}$$

To incorporate V into the energy function U, we assign a rest volume V_0 equal to the value in the elongated mesh. We then include

$$U_V = k_V(V - V_0)^2 \tag{4}$$

in the energy during minimization.

It is possible that there is resistance to torsion within the *Spirostomum* cortex. For instance, this could be contributed by the cortical microtubule bundles, which undergo some additional bending if there is twist between vertically adjacent layers of the mesh. To recapitulate this behavior, we treat adjacent layers as torsional springs. These springs penalize the relative twist $\Delta\psi_l$ and vertical separation Δz_l between adjacent layers l and $l+1$. The energy for the l^{th} layer is

$$u_l^{MT} = \frac{k_z}{2}(\Delta z_l)^2 + \frac{k_\psi}{2}(\Delta\psi_l)^2 + k_c \Delta z_l \Delta\psi_l \tag{5}$$

where k_c allows for coupling between stretching and twisting [17, 19]. The total energy of the microtubule is then a sum over the layers $\mathcal{L}$.

$$U_{MT} = \sum_{l \in \mathcal{L}} u_l^{MT}. \tag{6}$$

The stiffness parameters k_ψ, k_c, and k_z also scale inversely with the initial separation Δz^0 between layers, but because $\Delta z^0 = 8.2$ μm is approximately constant throughout the elongated mesh, we directly parameterize the stiffness values. In this paper, we set $k_c = k_z = 0$ and focus on the effect of k_ψ in resisting the untwisting of adjacent layers in the equatorial mesh, but future work could explore the dependence of this coupling term on the dynamics of contraction and twisting of *Spirostomum*.

The total energy function is

$$U(\{\mathbf{p}_i\}_{i=1}^N; \mathcal{K}) = U_S + U_V + U_{MT}. \tag{7}$$

To mimic the effect of calcium activation, we set the new spring rest lengths and numerically minimize the energy function with respect to the points $\mathbf{p}_i$. To exclude edge effects, only the middle 95% of layers contribute to U_{MT} and

have their rest lengths changed during contraction. Additionally, only the edges of these middle layers are rotated when converting the equatorial mesh into the fishnet mesh.

To parameterize the model, the size of the organism was estimated at approximately $100 \times 1,000$ μm in width and length. The initial twist of the mesh was also estimated from experimental images. Volume stiffness k_V was set high enough to ensure essentially perfect volume conservation. Bottom-up parameterization in terms of protein-level information is challenging because of the highly coarse-grained nature of the model. As a result, default values for the remaining parameters were found by searching parameter space for minimized structures that reasonably matched experimental images. We then explored nearby regions of these default values to study the effect of these parameters on the observed behavior (Fig. 2). The default parameters are reported in Table S1.

To quantify changes in concavity, we projected the 3D structure onto the longitudinal plane through the center of the structure and computed the projected area A_p in this plane. We then found the area of the projected shape's convex hull A_h and computed the inflection ratio $R_{ph} = A_p/A_h$, which will be less than 1 for a non-convex structure.

AlphaFold predictions of Sfi1 and centrin structures

Putative centrin and Sfi1 protein sequences from *Spirostomum* were identified after transcriptome assembly of RNA-seq data deposited at the NCBI SRA database for *Spirostomum* (SRX8646480 and SRX7201124) using Trinity running on the Galaxy server [20, 21]. The predicted transcripts were translated using the Virtual Ribosome server using Translation Table 10 (euplotid nuclear genetic code) [22]. This transcriptome will be reported in future work. The BLAST software package was used to search the derived proteome database for centrin and Sfi1 candidates using sequences from other ciliates as queries. The first candidates for Sfi1-like proteins were obtained using the *Paramecium tetraurelia* centrin-binding protein as a query (GenBank: CAI39100.2), which identified several proteins that contain multiple tandem repeats of the 69 amino acid sequence. Of these several candidate transcripts, we chose particularly long ones for further structural and sequence analysis; two representative example sequences are shown in Tables S3 and S2. We performed self-alignments of these predicted *Spirostomum* Sfi1 sequences, as well as the previously reported *S. cerevisiae* Sfi1 sequence, using the MPI Bioinformatics toolkit [23, 24] (Tables S4, S2, and S3). *S. cerevisiae* sequences were taken from the Saccharomyces genome database, SGD:S000003926 [25] using the Sfi1 repeat sequence previously identified by Li et al. (K246-E677) [26]. Close homologs of these proteins were also identified in the *Stentor* proteome and derived proteomes for other species of *Spirostomum* and *Bursaria*. *Spirostomum* centrin and five Sfi1 repeat sequences (Table S3) were used as input for ColabFold v1.5.5: AlphaFold2 using the MMseqs2 bot individually and in combination, as well as the Alphafold3 server hosted at alphafoldserver.com [27–30]. The initial models were relaxed using the built-in Amber software. Predicted structures were analyzed and visualized using the UCSF Chimera software [31].

SUPPLEMENTAL FIGURES

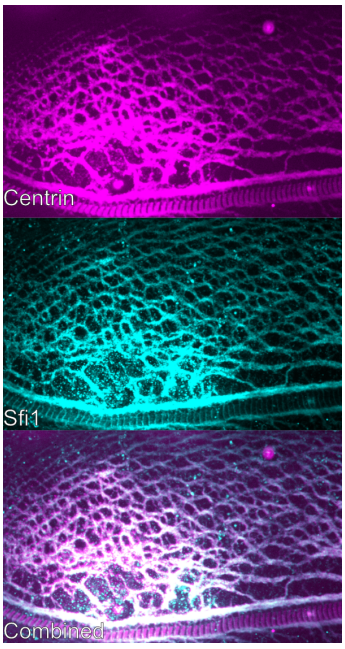

FIG. S1. Colocalization of Sfi1 and Centrin in elongated *Spirostomum* Top: Centrin (20H5) is shown in magenta, Middle: Sfi1 (custom peptide antibody against RTEKLRNALNRVPR), Bottom: combined image.

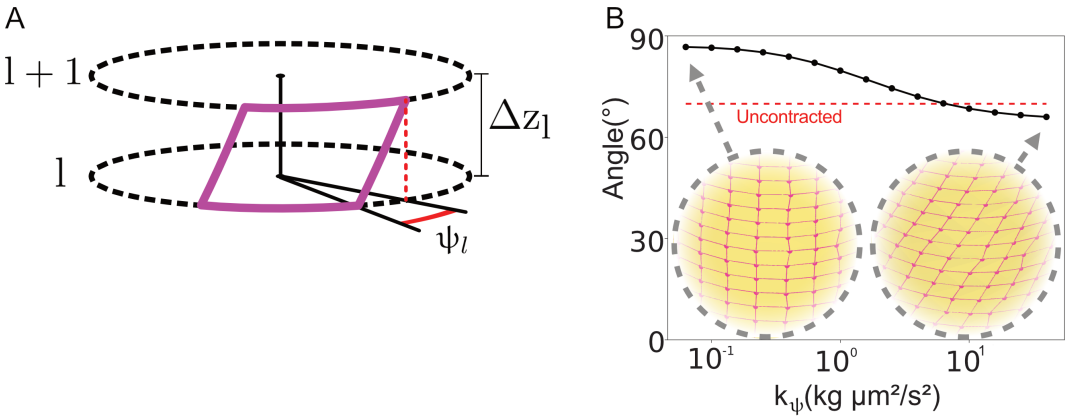

FIG. S2. Graphical Depiction of angle ψ and changes in ϕ with force applied in the latitudinal mesh model. **A** ψ is the angle measured between layers of the mesh as depicted here. **B** Contracted helix angle ϕ_C as the angular stiffness k_ψ is varied. The angle of the *elongated* helix ϕ_E is shown for comparison in red. Insets show mesh structures for example values of k_ψ.

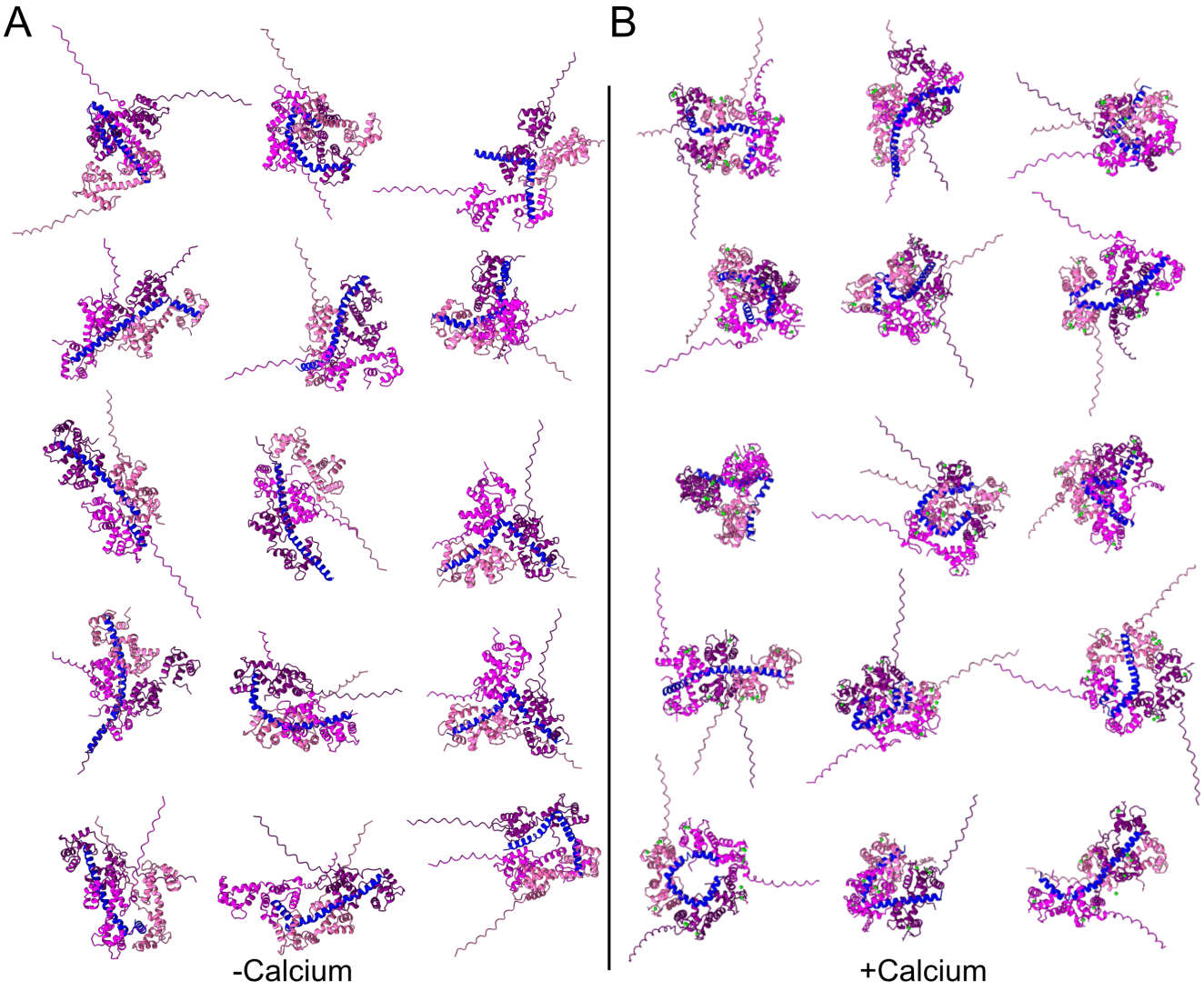

FIG. S3. Additional Alphafold3 predictions of centrin-Sfi1 complex with and without calcium ions. Alphafold modeling of one sfi1 repeat (blue), with 3 centrin molecules (magenta hues), with and without 12 additional calcium ions (green). **A** Predictions without calcium. **B** Predictions with 12 calcium ions. Models are aligned to best show the conformation of the Sfi1 repeat. Structure files are provided in Supp. Data 7.

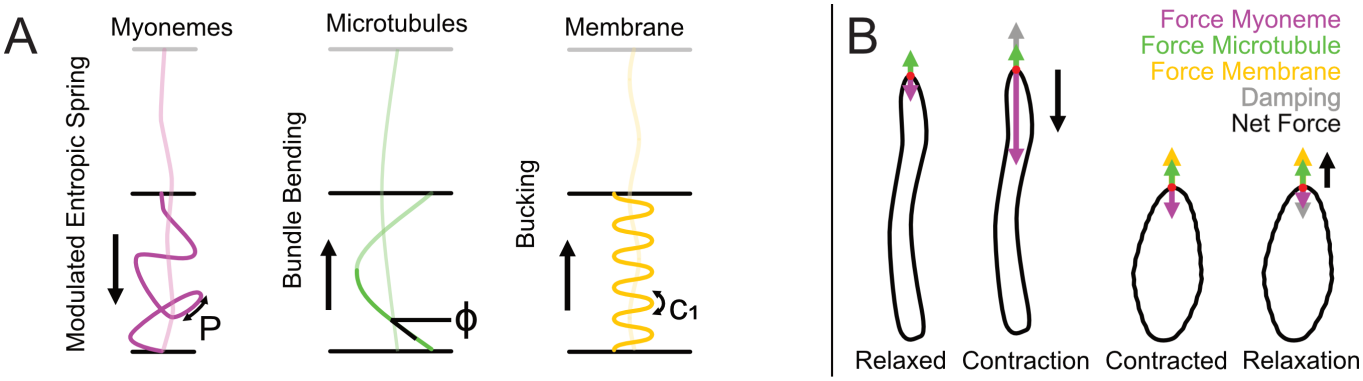

FIG. S4. Overview of forces estimated in the *Spirostomum* cortex. **A** Cartoon of forces estimated (left to right): myoneme (magneta), estimated as an entropic spring; microtubules (green) estimated via their bending moduli; and membrane curvature (gold) estimated via buckling force. **B** Cartoon of the relative magnitudes and net forces acting on *Spirostomum* over a contraction cycle. In the relaxed state, we predict that relatively little force is generated by the myoneme, which balances with the relatively small forces we estimate are contributed by the microtubules and membrane. During contraction, the myoneme generates large forces opposed primarily by drag (damping). In the fully contracted state, the organism is again briefly at equilibrium, when we predict that the myoneme generates relatively small forces compared to those it generates during the contraction phase. During relaxation, we predict that the net force likely requires unknown contributors, since we estimate that the forces from bending the microtubules and membrane are relatively small. Note arrows are not to scale, and only indicate qualitatively relative magnitude.

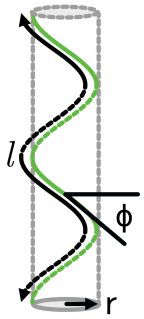

FIG. S5. Parameters for calculating microtubule bending energy. The microtubule bundles (green) form a helix around the cortex of *Spirostomum*, here approximated as a cylinder. Figure indicates the helical angle of the microtubule bundle ϕ, the radius r, and the total length of the microtubule bundle l .

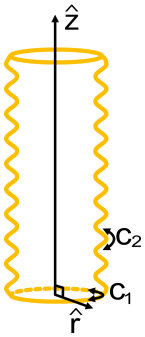

FIG. S6. Parameters for calculating membrane buckling energy. The membrane is approximated as a cylinder with sinusoidal walls. The z-axis (through the middle of the cylinder) and the r-axis (radial to cylinder) are shown. Curvature c_1 is in the plane perpendicular to $\hat{z}$ and is $1/r$ where r is the average radius of the cylinder. Curvature c_2 is in the $\hat{r}$ plane, along the sinusoidal ridges, and is estimated as the curvature of the sin function.

SUPPLEMENTAL TABLES

Parameter	**Symbol**	**Value**
Structure radius	R	50 µm
Structure length	L	980 µm
Elongated helix angle	ϕ_E	58°
Myoneme stiffness per length	EA	0.01 kg µm/s^2
Equatorial shrinking factor (LM)	γ_e	0.8
Longitudinal shrinking factor (LM)	γ_l	0.4
Left-handed shrinking factor (FM)	$\gamma_{l.h.}$	0.35
Right-handed shrinking factor (FM)	$\gamma_{r.h.}$	0.35
Twisting stiffness (LM)	k_ψ	2.0 kg µm^2/s^2
Twisting stiffness (FM)	k_ψ	0.0 kg µm^2/s^2
Volume conservation stiffness	k_V	10^9 kg/µm s^2

TABLE S1. Default parameters for the mesh model LM: Latitudinal mesh, FM: fishnet mesh

ID	Prob	P-val	Loc	Sequence
A1	98.76	2.5e-23	1-51	----------PKSALAKWRQFVDDIKKGRILNAVKAQKLATSLTKIPVRKLKDANDRIIGG
A2	99.86	1.5e-28	52-120	GSKVKGVLKGIMKKLSDKPKSAFAKWRKFVDDIKKGKVLDAVKAQKLAVCLAKIPVRRLKDANDRIIGG
A3	99.25	3.1e-24	121-189	GSKIKGVLRGIMKKLSERPKSAFAKWRAYIDSVKKGKILDAVKAQKLAASLRKIPVRRLKDANDRILGG
A4	99.71	7.4e-27	190-258	GSKVAGVLRGIMKKLKDKPKSALAKWRDFVDNIKKGKILNAVKAQKLAVCLAKIPVRRLKDANDRIIGG
A5	99.62	3.0e-26	259-327	GSKIAGVLRGIMKKLKDKPKSAFAKWRQFIEDIKKGKVLDAVKAQKLASCLTKIPVRKLKDANDRIIGA
A6	99.67	1.5e-26	328-396	GSKVAGVLRGIMKKLKDKPKCALARWRQYVDEVKKGKVLDAVKAQKLAASLNRIPVRIMKDANDRILGD
A7	99.60	4.7e-26	397-465	GSKIKGVLRGIMKKLAEKPKKAFARWRAFVDDIKKGKVLDAVKAQKLAACLAKIPVRRLKDANDRILGG
A8	99.52	1.4e-25	466-534	GSRIAGALRGIMKKLKDKPKSALARWRQFVEDIKKGKVLDAVKAQRLAASLSKIPTRRLKDANDRIIGG
A9	99.34	9.8e-25	535-603	GSKVAGVLRSIMSRLKEKPKSAFTKWRAFVNDIKKGRMLNAVKAQQLVVSLSKIPIRRLKDANDRIIGG
A10	99.70	8.4e-27	604-672	GSKIKGVLRAILKKLKDKPKSALAKWRTFVDDIKKGKVLDAVKAQKLAACLARIPVRRLKDANDRVIGG
A11	99.78	1.5e-27	673-741	GSKIKGVLRSIMKKLSDKPKSAIARWRQFVDDIKKGKVLDAVKAQKLASCLARIPNRIVRDANDRILGD
A12	99.10	9.8e-24	742-810	GSKVKGALRALVKKLSDKPKTALKKWKQFVDDVKKGKVLDAVKAQKLVVALSRVPIRIVKDANERILGG
A13	99.64	2.9e-26	811-879	GNKVKGALRSLVHKLAQKPKSALSKWRQFVEDVKKGKVLDAVKAQKLASTLSRVPARVVRDANDRILGG
A14	99.57	7.0e-26	880-948	GDKVKGALRALVHKLSQKPKLALSKWRSFVEGVKKGRILDAVKAQKLAKSLSRVPLRTVKDANDRVIGG
A15	99.67	1.4e-26	949-1017	GNKVKGALRNLMHKLIQKPRQALEKWKQYVENVKRGKILDQVKVQKLKASLIRVVTRTLFPAFKAATGM
A16	97.73	3.4e-19	1018-1068	PTLIKSMLRNLAHIIDATPRNALSRWRSAIASSKHNAAQESLKNVLRAIKF----------

TABLE S2. *Spirostomum* Sfi1 15 repeat self-alignment. Conserved tryptophans shown in green. Helix breaking residues (proline and glycine) shown in blue. Probabilities and p-values for the alignment were calculated using MPI Bioinformatics Toolkit (see Supp. Materials and Methods).

ID	Prob	P-val	Loc	Sequence
A1	99.99	1.2e-33	1-67	--PKQALERWKDYVASIKGKKMLDAVKAQKLQHHLQSIPSRKLKDATERVIGNADKVKGALRSLVHKLA
A2	99.99	7.1e-34	68-136	QKPRDALARWKRYVDAVKKGKVLDQVNAAKLITAMTRVPNRVLRDATERMFGDGSKLKGALRSLLHKLS
A3	99.99	3.1e-34	137-205	QKPKNALAQWKKYADAVKCGKVLDQVKASKLMTALTQVPNRVLKDATDRVFGDGSKLKGAMRSLLHKLS
A4	99.99	2.1e-34	206-274	QKPKDALAKWKKYVEAIKKGKVLDQVNAAKLVTALAQIPNRVLNDANERILGDGSKLKGAMRSLLKKLS
A5	99.98	5.4e-31	275-342	QKPKDALEKWRKYVDAVKRGKVLDQVKASKLLAALTKVPNRLLKDATERIVGEGSKLKGALKSLLKKL-

TABLE S3. *Spirostomum* Sfi1 5 repeat segment self-alignment used in Alphafold modeling (Fig. 5, S3). Conserved tryptophans shown in green. Helix breaking residues (proline and glycine) shown in blue. Probabilities and p-values for the alignment were calculated using MPI Bioinformatics Toolkit (see Supp. Materials and Methods).

ID	Prob	P-val	Loc	Sequence
A1	82.33	7.6e-08	12-37	---SFRNTWLLFRSFQ.QWITLTQTLKEQS.....
A2	80.10	1.2e-06	38-58	---RLADQAFLNKMFR.KILKAQEH-----WKHLET.....
A3	84.69	5.0e-08	65-87	VNTDNIKKIFLRTTFH.IWKLRHK------EINY.....
A4	72.88	1.0e-05	92-108	-------HGLERRIFE.RIKQKVIN-----YEYNKS.....
A5	84.82	6.3e-08	115-138	IAEKVRSFSLQRKYLN.KWEKKNIE-----NEDKLG.....
A6	83.77	3.9e-07	145-168	ALYELENKFIKQKFFR.KLNRSFQH-----SQQEAIAKS....
A7	80.63	1.3e-06	178-198	----KLNQTLLRCVFEKMWLKRFED-----HLHLYS.....
A8	81.62	1.3e-06	205-232	-IVSLKEANLVKRIFH.SWKKLLYIDLKAS.....
A9	82.30	7.1e-08	233-253	---DYSRTNLLKSSLR.SWKLEVKL-----KIFEQ.....
A10	79.51	2.9e-06	259-283	----KCKKSIQASAYR.TWRKRIQYGKISS.....
A11	80.86	3.1e-06	284-304	---EHVKTAFCAKYLG.VWKRRMLQ-----MNSMND.....
A12	83.58	3.1e-07	311-339	EASKFYEEGLVNECLA.IWKERLIKTKELE.....
A13	76.34	7.4e-05	340-360	---DRYNFLCKTHAIL.TVKRTLMH-----IDNVHLLYTKLAP
A14	79.77	2.4e-06	374-393	----SMDRVKLSKAFL.KWRKATRF-----KVRHKLNDILHVY
A15	81.82	7.5e-07	407-427	--EKSKERELQSQLFN.AWRNRFC------.....

TABLE S4. *S. cerevisiae* Sfi1 15 repeat K246-E677 self-alignment [26]. Loc 1 is residue K246. Conserved tryptophans shown in green. Helix breaking residues (proline and glycine) shown in blue. Probabilities and p-values for the alignment were calculated using MPI Bioinformatics Toolkit (see Supp. Materials and Methods).

SUPPLEMENTAL DATA

The following files are included as data referenced in this study.

	File Name	Description
1	`Yeast_3rp_AF2.pdb`	Representative Alphafold2 prediction for 3 *S. cerevisiae* Sfi1 repeats (equivalent to 1 *Spirostomum ambiguum* repeat).
2	`Spiro_5rp_AF2.pdb`	Representative Alphafold2 prediction for 5 *Spirostomum ambiguum* Sfi1 repeat.
3	`Yeast_15rp_AF2.pdb`	Representative Alphafold2 prediction for 15 *S. cerevisiae* Sfi1 repeat (equivalent to 5 *Spirostomum ambiguum*).
4	`Spiro_1rp_AF2.pdb`	Representative Alphafold2 prediction for 1 *Spirostomum ambiguum* Sfi1 repeat.
5	`Spiro_3Centrin_Sfi1_12Ca_AF3.pdb`	Alphafold3 prediction of 3 centrin binding to Sfi1 in the presence of calcium.
6	`Spiro_3Centrin_Sfi1_AF3.pdb`	Alphafold3 prediction of 3 centrin binding to Sfi1 in the absence of calcium.
7	`Spiro_1rpSfi1_3cen_+-Ca_30runs.pdb`	Additional Alphafold3 predictions of 1 Sfi1 repeat with 3 centrins 30 total complexes.

Spirostomum ambiguum Centrin Sequence

`MAGRAPASKAGPPAAKAGPPAFNAKRYERPGLTEDEIEEIKEAFDLFDTDGSGTIDPKELKSAMESLGFEAKNQTIYQMISDLDKDGSGAIDFDEFL`
`DMMTARLSDKDSRDDINKVFRLFDDEKQGFITIKNLRRVAKELGETMTDEELLEMIERADSDGDGRVTAEDFYNIMTKKAFP`

SUPPLEMENTAL DISCUSSION

1. Energetics and total force calculations

In this section, we estimate the mechanical energy stored in and forces exerted by structures in the *Spirostomum* cortex (Fig. S4). Starting with our imaging results shown in the main text and previously measured mechanical parameters, we estimate energies stored in cortical microtubule bundles and the membrane and use these estimates to make predictions about the force exerted by the myonemes.

Microtubule bending energy estimation

As shown in Fig. 1, the microtubules in the cortex of *Spirostomum* form large helical coils, similar in shape to a spring. During contraction, these coils compress, which could potentially result in the storage of energy from contraction in microtubule bending. We used previous measurements of the mechanical properties of microtubules to estimate the total energy stored in this bending.

The elastic energy stored in a single microtubule curled into a transverse coil (Fig. S5) is given by

$$E = \frac{\kappa l}{2r^2} cos^4(\phi) \tag{8}$$

where E is the total elastic energy in the coil, κ is the bending stiffness of the microtubule, l is the total length of the microtubule, r is the radius of the coil, and ϕ is the complement of the pitch angle of the coil (we have reframed Eqn. B2 from [32] to match the angle as we have defined it in Fig. 1A). For a bundle of microtubules, we expect this energy to scale linearly with the number of microtubules in the bundle.

In the calculations below, we use the following estimated parameters (based on imaging data from elongated *Spirostomum* as in Fig. 1 and previously published measurements of microtubule mechanics):

$\kappa \approx 10\,\mathrm{pN\,\mu m^2}$ [32–34]

$r \approx 35\,\mu\mathrm{m}$

$l \approx 900\,\mu\mathrm{m}$

$\phi \approx 64^\circ$

≈ 150 microtubules per bundle [35] and ≈ 50 bundles in the organism.

Plugging in these values, we find

$$E \approx 1.0\,\mathrm{fJ}. \tag{9}$$

In contracted *Spirostomum*, we estimate the following changes to these parameters (those not listed are unchanged):

$r \approx 60\,\mu\mathrm{m}$

$\phi \approx 34^\circ$

Plugging in these values, we find

$$E \approx 4.4\,\mathrm{fJ}. \tag{10}$$

Per microtubule this works out to be $\sim 1 \times 10^{-4}\,\mathrm{fJ}$. Notably, since the radius of the organism expands during contraction while the helical pitch decreases, there is relatively little resulting change in energy stored in microtubule bending. Compared to the amount of energy expended to cause organismal contraction (see below), we thus expect microtubules to have a negligible contribution toward opposing contraction.

Membrane buckling energy estimation

In the contracted state, we observe periodic ripples in the membrane (Fig. 1). To measure the potential effect of membrane buckling during contraction and determine if the membrane stores significant energy from contraction for use in elongation, here we estimate the energy expended into the membrane to form these ridges.

The energy of bending for a membrane is given by

$$E_m = \iint \frac{1}{2} K_b (c_1 + c_2 - c_0)^2 + \bar{K} c_1 c_2 \, dA \tag{11}$$

where c_1 and c_2 are the principal curvatures, and c_0 is the spontaneous curvature, K_b is the bending rigidity and $\bar{K}$ is the Gaussian bending modulus (Helfrich theory [36, 37]). We approximate *Spirostomum* as a wavy cylinder with a sinusoidal curve that varies along the long axis of the cylinder (Fig. S6). The curvature c_1 is defined by the radius of this cylinder, whereas c_2 is caused by the membrane ridges. We are actually interested in the *change* in bending energy during contraction, and assume that it is dominated by c_2, which in the contracted state is much larger than c_1. We also assume that, while the spontaneous curvature c_0 may be non-zero, it is still much smaller than c_2. However, we acknowledge that there may be some mechanisms for manipulating spontaneous curvature that are yet unknown in *Spirostomum*, and that such mechanisms might be useful in inducing the changes in shape we observe.

Thus, we now want to evaluate

$$\Delta E_m \approx \iint \frac{1}{2} K_b c_{2,c}^2 \, dA \tag{12}$$

where the subscript c indicates the contracted state. To find $c_{2,c}$, we consider the surface described above, which is defined by

$$r = r_0 + \alpha \cdot sin(\omega z) \tag{13}$$

where α is the amplitude of the sinusoidal wave, ω is its angular frequency, and r_0 is the average radius of the organism. The curvature of this function is

$$c_{2,c} = \frac{\alpha w^2 \sin(wz)}{(1 + \alpha^2 \omega^2 \cos^2(wz))^{\frac{3}{2}}}. \tag{14}$$

We now take advantage of the periodicity of this function by evaluating the integral in z over a single period and scaling up to the entire organism:

$$\Delta E_m \approx \frac{1}{2} K_b \iint c_{2,c}^2 \, dA = K_b r L \frac{\omega}{2} \int_0^{2\frac{\pi}{\omega}} c_{2,c}^2 dz \tag{15}$$

where L is the length of the organism and r is its radius. This integral evaluates to:

$$\frac{\alpha^2 w^4 (4 + 3\alpha^2 \omega^2)}{8(1 + \alpha^2 \omega^2)^{\frac{3}{2}}} \tag{16}$$

resulting in

$$\Delta E_m \approx \frac{1}{2} K_b \Big(\frac{\alpha^2 \omega^4 (4 + 3\alpha^2 \omega^2)}{8(1 + \alpha^2 \omega^2)^{\frac{3}{2}}} \Big) \cdot 2\pi r L \tag{17}$$

To estimate the value of this expression, we use the following parameters (from previous measurements and imaging as in Fig. 1):

$K_b \approx 1 \times 10^{-19}$ J [38]

$r_c \approx 50\,\mu$m

$\alpha \approx 1\,\mu$m

$\omega \approx \frac{2\pi}{2\,\mu\text{m}}$

$L \approx 1\,\mathrm{mm}$

$$\Delta E_m \sim 100\,\mathrm{fJ} \tag{18}$$

While this energy is somewhat larger than what we estimate is stored in microtubule bending, it is still not a significant source of energy storage compared to that expended in contraction.

Estimate of force exerted by individual myoneme filament bundles

We can now compare our estimates of the mechanical contribution of the microtubules and membrane to previous measurements of the force generated during contraction. Using a glass needle to hold *Spirostomum* in an elongated state, Hawkes et al. measured the force generated by *Spirostomum* contraction to be 5×10^{10} pN [39]. This important measurement was done in an isometric state, where enough force was exerted to prevent contraction. To get a rough estimate of the energy expended during contraction, we can multiply this force by the change in length, i.e.,

$$E = \int F \cdot dl \approx F \cdot \Delta l.$$

With a change in length of 1000 µm, this results in an estimate of the work done by the myoneme of:

$$E_{myoneme} \approx 1 \times 10^5\,\mathrm{fJ}.$$

This value is at least 3 orders of magnitude larger than either our estimate of the energy required to bend the membrane into the folds or our estimate of the bending energy of microtubules in the contracted state. Thus, we conclude that neither microtubules nor membrane bending meaningfully oppose contraction, nor induce elongation.

We can also use this measurement of the organismal force to estimate the force generated by individual myoneme bundles. Taking the myoneme as a mesh of springs, some in parallel and some in series, we find

$$F_{total} = N_{\mathrm{parallel}} \cdot F_{\mathrm{bundle}} + \frac{F_{\mathrm{bundle}}}{N_{series}}$$

where N_{parallel} and N_{series} are the number of bundles that effectively act in parallel and in series, respectively, and F_{bundle} is the force produced by a single myoneme bundle. While none of the individual myonemes are perfectly in series or in parallel, we can estimate their effective action from the aspect ratio of the contracted *Spirostomum* so that

$$\frac{N_{\mathrm{parallel}}}{N_{\mathrm{series}}} = \frac{\mathrm{length}}{\mathrm{circumference}}.$$

Note that as *Spirostomum* contracts this ratio will change; this means that in the contracted state, myonemes are generating fractionally less force along the long axis. We can verify this effect by examining the immunofluorescence images, where indeed the myoneme filaments make a greater angle to the long axis in the contracted state, meaning they will contribute less force in the longitudinal direction. To estimate this ratio, we will use the elongated values since Hawkes et al. found the largest force in more elongated states [39]:

$$\frac{N_{\mathrm{parallel}}}{N_{\mathrm{series}}} \approx \frac{1000\,\mu\mathrm{m}}{2\pi \cdot 35\,\mu\mathrm{m}}$$

$$\frac{N_{\mathrm{parallel}}}{N_{\mathrm{series}}} \approx 4.5.$$

We can now estimate the total number of myonemes ($N = N_{\mathrm{parallel}} + N_{\mathrm{series}}$) using the area of a unit of the myoneme mesh and dividing by the total organismal surface area. We must then multiply by two since there are two sides contributed per unit so that

$$N \approx \frac{4\pi r h}{a_E b_E \cdot cos(\Phi_E)}.$$

Using the elongated size as 1000 µm long by 35 µm in radius, and taking a_E, b_E, and ϕ_E from Fig. 1, we find

$$N \approx 8 \cdot 10^4.$$

We can now solve F_{total} in terms of the ratio and total:

$$F_{\text{total}} \approx F_{\text{bundle}} \left(\frac{N_{\text{total}} \cdot \frac{N_{\text{parallel}}}{N_{\text{series}}}}{1 + \frac{N_{\text{parallel}}}{N_{\text{series}}}} + \frac{1 + \frac{N_{\text{parallel}}}{N_{\text{series}}}}{N_{\text{total}}} \right).$$

Plugging in our previously estimated values we find that

$$F_{\text{bundle}} \approx 10\,\text{pN}.$$

Estimate of persistence length of contracted myoneme given force

Finally, we estimate the change in persistence length of the contracted myoneme fiber that could produce the force estimated in the previous section. From TEM experiments, we estimate that the elongated myoneme fibers have a persistence length of the order 100 nm (Fig. 4). Alphafold predictions (Fig. 5) suggested a molecular mechanism where centrin-calcium interactions modulate the persistence length to produce contraction. Here, we validate that these proposed dynamics could reasonably generate the forces in each filament bundle by calculating the persistence length needed to generate these forces.

To first order WLC model gives an estimate of the force to be

$$F_{\text{filament}}(x) = \frac{k_B T}{P} \left(\frac{1}{4\left(1 - \frac{x}{L}\right)^2} - \frac{1}{4} + \frac{x}{L} \right)$$

where P is the persistence length, k_b is the Boltzmann constant, T is the temperature, L is the total length, and x is the displacement from equilibrium. Here we are assuming that the elongated length has a relatively small force and is close to its rest length. Taking the change in rest length to be 27% (averaging changes in a and b as shown in Fig. 1D), so that $\frac{x}{L} = (1 - 0.27)$. Taking $T = 300K$, $F_{\text{total}} = 10pN$, and there being of order 100 filaments per bundle so that $F_{\text{filament}} = F_{\text{bundle}}/100$. We can estimate the persistence length of the contracted myoneme filament,

$$P_{\text{contracted}} \approx 10\,\text{nm}.$$

To validate the reasonableness of this number, we compare it to the measured persistence length of the myosin X lever arm, which forms a single alpha helix (SAH), similar to the structure we predict Sfi1 might form in contracted myonemes if binding of calcium causes centrin to partially detach (Fig. 5). This myosin X SAH domain has a previously measured persistence length of 10 nm, remarkably similar to our estimate [40, 41]. Thus, entropic-spring powered shortening of myoneme fibers, driven by an approximately 10-fold reduction in the persistence length of an Sfi1 filament, is a reasonable mechanism of *Spirostomum* contraction.

2. Latitudinal mesh model

We find that in the latitudinal model the closed-loop strands of myoneme lead to local pinching around the equators and create inflection points where the structure is no longer convex. In Fig. 2C we show a heatmap of the inflection metric (which is less than 1 for non-convex shapes; see Materials and Methods) as we vary the myoneme spring shrinking factors γ_l, γ_e of longitudinal and equatorial myoneme strands. This figure reveals a critical line in the γ_l, γ_e space over which the structure loses convexity due to greater shrinkage in the equatorial direction relative to the longitudinal direction. To achieve appreciable contraction in the organism's length, the shrinking in the equatorial direction must be significantly less than in the longitudinal direction; this condition is likely non-physiological since it would require systemic differences in myoneme structure or biochemistry depending on their angle. Furthermore, we find that in the equatorial mesh the adjacent equatorial strands are free to untwist relative to each other and will do so unless explicitly penalized by the torsional penalty (Fig. 2G). Even under stiff torsional rigidity, the helix angle in the contracted equatorial mesh is much larger than experimentally observed.

SUPPLEMENTAL REFERENCES

[1] R. H. Whitten and W. R. Pendergrass, *Carolina protozoa and Invertebrates Manual* (Carolina Biological Supply Co., 1980).
[2] M. Schliwa and J. van Blerkom, J. Cell Biol. **90**, 222 (1981).
[3] C. Guerra, Y. Wada, V. Leick, A. Bell, and P. Satir, Molecular Biology of the Cell **14**, 251–261 (2003).
[4] M. J. Dykstra and L. E. Reuss, *Biological Electron Microscopy: Theory, Techniques, and Troubleshooting* (Springer Science & Business Media, 2011).
[5] J. Kuo, *Electron Microscopy: Methods and Protocols* (Springer Science & Business Media, 2008).
[6] R. S. Petralia and Y.-X. Wang, Front. Neuroanat. **15**, 763427 (2021).
[7] E. M. Sciences, Post-embedding Immuno Incubation Protocol, `https://www.emsdiasum.com/docs/technical/techtips/em_protocolpost`, accessed: 2023-4-3.
[8] J. Schindelin, I. Arganda-Carreras, E. Frise, V. Kaynig, M. Longair, T. Pietzsch, S. Preibisch, C. Rueden, S. Saalfeld, B. Schmid, J.-Y. Tinevez, D. J. White, V. Hartenstein, K. Eliceiri, P. Tomancak, and A. Cardona, Nat. Methods **9**, 676 (2012).
[9] J. D. Hunter, Computing in science & engineering **9**, 90 (2007).
[10] M. Waskom, O. Botvinnik, D. O'Kane, P. Hobson, S. Lukauskas, D. C. Gemperline, T. Augspurger, Y. Halchenko, J. B. Cole, J. Warmenhoven, J. de Ruiter, C. Pye, S. Hoyer, J. Vanderplas, S. Villalba, G. Kunter, E. Quintero, P. Bachant, M. Martin, K. Meyer, A. Miles, Y. Ram, T. Y. aid Mike Lee Williams, C. Evans, C. Fitzgerald, Brian, C. Fonnesbeck, A. Lee, and A. Qalieh, Zenodo 10.5281/zenodo.883859 (2017).
[11] S. Berg, D. Kutra, T. Kroeger, C. N. Straehle, B. X. Kausler, C. Haubold, M. Schiegg, J. Ales, T. Beier, M. Rudy, K. Eren, J. I. Cervantes, B. Xu, F. Beuttenmueller, A. Wolny, C. Zhang, U. Koethe, F. A. Hamprecht, and A. Kreshuk, Nature Methods 10.1038/s41592-019-0582-9 (2019).
[12] T. Kluyver, B. Ragan-Kelley, F. Pérez, B. Granger, M. Bussonnier, J. Frederic, K. Kelley, J. Hamrick, J. Grout, S. Corlay, P. Ivanov, D. Avila, S. Abdalla, and C. Willing, in *Positioning and Power in Academic Publishing: Players, Agents and Agendas*, edited by F. Loizides and B. Schmidt (IOS Press, 2016) pp. 87 – 90.
[13] G. Bradski, Dr. Dobb's Journal of Software Tools (2000).
[14] R. Phillips, J. Kondev, J. Theriot, H. G. Garcia, and N. Orme, Physical Biology of the cell 10.1201/9781134111589 (2012).
[15] C. Floyd, A. T. Molines, X. Lei, J. E. Honts, F. Chang, M. W. Elting, S. Vaikuntanathan, A. R. Dinner, and M. S. Bhamla, Proceedings of the National Academy of Sciences **120**, 10.1073/pnas.2217737120 (2023).
[16] E. Catmull and J. Clark, Computer-aided design **10**, 350 (1978).
[17] O. M. O'Reilly, *Modeling nonlinear problems in the mechanics of strings and rods* (Springer, 2017).
[18] H. Ni and G. A. Papoian, The Journal of Physical Chemistry B **125**, 10710 (2021).
[19] J. Gore, Z. Bryant, M. Nöllmann, M. U. Le, N. R. Cozzarelli, and C. Bustamante, Nature **442**, 836 (2006).
[20] M. G. Grabherr, B. J. Haas, M. Yassour, J. Z. Levin, D. A. Thompson, I. Amit, X. Adiconis, L. Fan, R. Raychowdhury, Q. Zeng, Z. Chen, E. Mauceli, N. Hacohen, A. Gnirke, N. Rhind, F. di Palma, B. W. Birren, C. Nusbaum, K. Lindblad-Toh, N. Friedman, and A. Regev, Nat Biotechnol **29**, 644 (2011).
[21] T. G. Community, Nucleic Acids Res. **50**, W345 (2022).
[22] R. Wernersson, Nucleic Acids Research **34**, W385 (2006), https://academic.oup.com/nar/article-pdf/34/suppl_2/W385/7623425/gkl252.pdf.
[23] F. Gabler, S. Nam, S. Till, M. Mirdita, M. Steinegger, J. Söding, A. N. Lupas, and V. Alva, Current Protocols in Bioinformatics **72**, 10.1002/cpbi.108 (2020).
[24] L. Zimmermann, A. Stephens, S.-Z. Nam, D. Rau, J. Kübler, M. Lozajic, F. Gabler, J. Söding, A. N. Lupas, and V. Alva, Journal of Molecular Biology **430**, 2237–2243 (2018).
[25] P. Ma, J. Winderickx, D. Nauwelaers, F. Dumortier, A. De Doncker, J. M. Thevelein, and P. Van Dijck, Yeast **15**, 1097 (1999).
[26] S. Li, A. M. Sandercock, P. Conduit, C. V. Robinson, R. L. Williams, and J. V. Kilmartin, The Journal of Cell Biology **173**, 867–877 (2006).
[27] M. Mirdita, K. Schütze, Y. Moriwaki, L. Heo, S. Ovchinnikov, and M. Steinegger, Nature Methods **19**, 679–682 (2022).
[28] M. Varadi, S. Anyango, M. Deshpande, S. Nair, C. Natassia, G. Yordanova, D. Yuan, O. Stroe, G. Wood, A. Laydon, and et al., Nucleic Acids Research **50**, 10.1093/nar/gkab1061 (2021).
[29] J. Jumper, R. Evans, A. Pritzel, T. Green, M. Figurnov, O. Ronneberger, K. Tunyasuvunakool, R. Bates, A. Žídek, A. Potapenko, and et al., Nature **596**, 583–589 (2021).
[30] J. Abramson, J. Adler, J. Dunger, R. Evans, T. Green, A. Pritzel, O. Ronneberger, L. Willmore, A. J. Ballard, J. Bambrick, and et al., Nature **630**, 493–500 (2024).
[31] E. F. Pettersen, T. D. Goddard, C. C. Huang, G. S. Couch, D. M. Greenblatt, E. C. Meng, and T. E. Ferrin, J. Comput. Chem. **25**, 1605 (2004).
[32] M. Cosentino Lagomarsino, C. Tanase, J. W. Vos, A. M. C. Emons, B. M. Mulder, and M. Dogterom, Biophys. J. **92**, 1046 (2007).
[33] M. E. Janson and M. Dogterom, Biophysical Journal **87**, 2723–2736 (2004).
[34] M. C. Lagomarsino, C. Tanase, J. W. Vos, A. M. Emons, B. M. Mulder, and M. Dogterom, Biophysical Journal **92**, 1046–1057 (2007).
[35] H. Ishida, Y. Shigenaka, and M. Imada, Zoolog. Sci. (1988).
[36] Libretexts, 2.3: Membrane curvature (2022).

[37] F. Campelo, C. Arnarez, S. J. Marrink, and M. M. Kozlov, Advances in Colloid and Interface Science **208**, 25–33 (2014).
[38] R. Dimova, Advances in Colloid and Interface Science **208**, 225–234 (2014).
[39] R. B. Hawkes and D. V. Holberton, J. Cell. Physiol. **85**, 595 (1975).
[40] S. Sivaramakrishnan, B. J. Spink, A. Y. Sim, S. Doniach, and J. A. Spudich, Proceedings of the National Academy of Sciences **105**, 13356–13361 (2008).
[41] Y. Sun and Y. E. Goldman, Biophys. J. **101**, 1 (2011).